Materials Today Physics 27 (2022) 100792

Contents lists available at ScienceDirect

Materials Today Physics

journal homepage: www.journals.elsevier.com/materials-today-physics

Emerging exotic properties of two-dimensional ternary tetrahexagonal BCN: Tunable anisotropic transport properties with huge excitonic effects for nanoelectronics and optoelectronics

Mehmet Emin Kilic *, Kwang-Ryeol Lee **

Computational Science Research Center, Korea Institute of Science and Technology, Seoul, 02792, Republic of Korea

A B S T R A C T

A two-dimensional ternary tetrahexagonal BCN monolayer (*th*-BCN) is designed by applying Stone-Wales transformation to its pentagonal counterpart (*p*-BCN). Using first-principles calculations, we examine the dynamical, mechanical, thermal, and environment stability of *th*-BCN. The monolayer exhibits superior anisotropic electronic and optical properties compared to its counterparts (the domains of C and BN in the tetrahexagonal network and *p*-BCN). Direct band gap of 3.05 eV and excellent band edge alignment with the oxidation and reduction reactions of water heralds the use of *th*-BCN in photocatalytic water splitting. The band gap energy and band edge positions can be further adjusted by strain. The anisotropic high carrier mobility of *th*-BCN improves fast carrier separation and low recombination rate. The electronic transport direction can be easily controlled by strain engineering. For instance, one can rotate the preferred transport direction of hole by 90° with a very small uniaxial strain. Many-body effects beyond DFT reveal that the monolayer has strong light-harvesting capability ($10^5 cm^{-1}$) in the visible-ultraviolet region and exhibits strong excitonic effects with large excitonic binding energy of 0.98 eV. All these appealing properties make *th*-BCN a promising and tunable anisotropic 2D material for nanoelectronic and optoelectronic applications.

1. Introduction

The discovery of graphene (*h*-C) with its unique nano-scale properties has sparked significant interest in two-dimensional (2D) nanomaterials [1]. In recent years, various 2D materials including hexagonal boron nitride (*h*-BN) [2], transition-metal dichalcogenides [3], phosphorene [4], and others [5,6], have been successfully synthesized. Their unique properties offer exciting opportunities for many applications [7,8]. Such that, large surface area and ultra thin thickness make them desirable surface active materials for photocatalyst [9]. Furthermore, mechanical flexibility and optical transparency, arising from their atomic thickness, are highly promising for optoelectronic devices [10]. Moreover, the electrons in 2D materials are confined into planes, emerging exotic electronic properties for next-generation electronic devices.

Going beyond *h*-C, a new 2D carbon allotrope composed of five-membered rings, namely penta-graphene (*p*-C), has been proposed and received considerable attention due to its unique geometry and remarkable properties such as near zero negative Poisson's ratio and ultra-high ultimate strength [11]. A wealth of 2D pentagonal monolayers has emerged from unary to binary and ternary forms [12–15]. Remarkably, some of them, including *p*-$PdSe_2$ [16], *p*-PdS_2 [17], *p*-NiN_2 [18], and pentagonal silicene nanoribbons [19] have been realized in experiment.

Recently, by applying the Stone-Wales (SW) transformation to *p*-C, an energetically more favorable 2D carbon allotrope, namely tetrahexcarbon (*th*-C), has been predicted [20]. The *th*-C monolayer with superior switchable properties including sign-tunable Poisson's ratio, tunable phononic gap, sizable direct band gap, and anisotropic high carrier transport properties [21] is of great importance for functional electronic and photonic devices. Using a combinatorial substitutional search in *th*-C, many new binary and ternary tetrahexagonal compounds with novel properties have been recently predicted [22–25]. They offer great promising in the applications of nanoelectronics and optoelectronics. For instance, penta-carbides (*p*-XC_2, X = Si, Ge, Sn) with indirect band gaps and appropriate band edges have been predicted to hold great potential for photocatalytic water splitting [12] while their tetrahexagonal counterparts (*th*-XC_2) with narrow direct band gaps and anisotropic transport properties are ideal 2D materials for nanoelectronics [23]. Moreover, the *th*-CX_2 (X = P, As, Sb) compounds [25], tetrahexcarbides (*th*-XC, X = Si, Ge, Sn) [22] with suitable band gap and band edges positions and high optical absorption capability in the visible

* Corresponding author.
** Corresponding author
E-mail addresses: mekilic@kist.re.kr (M.E. Kilic), krlee@kist.re.kr (K.-R. Lee).

https://doi.org/10.1016/j.mtphys.2022.100792
Received 5 April 2022; Received in revised form 19 July 2022; Accepted 19 July 2022
Available online 1 August 2022
2542-5293/© 2022 Elsevier Ltd. All rights reserved.

range show excellent potential for photocatalytic water splitting. The *th*-BN with large band gap has been suggested to be a suitable substrate for tetrahexagonal structures [24]. Boron-pnictogens in tetrahexagonal lattice have been recently proposed as highly anisotropic 2D materials for nanoelectronics and optoelectronics [26].

Ternary alloying is a very promising modification strategy in 2D materials. Boron-carbon-nitrogen (BCN) monolayers composed of *h*-BN and *h*-C domains as unique recent class of 2D materials exhibit enormous potential as non-metallic catalysts because of the easy tunability of bandgap, surface area, and other electronic properties with variation in composition [27,28]. Zhao et al. predicted ternary pentagonal BCN (*p*-BCN) monolayer with novel properties such as spontaneous polarization and intrinsic piezoelectricity [29]. Furthermore, we have revealed its electronic and optical properties, and showed potential uses for photocatalytic water splitting, which are not observed the domain of C and BN in pentagonal lattice [30]. Very recently, Sharma et al. have showed the enhancement in the electronic and optical properties of *p*-BCN by fluorination [31]. Parallel to this achievements, Lopez-Bezanilla et al. predicted ternary BNSi and BCN monolayers using a combinatorial substitution search method in *th*-C [32].

Using first principles calculations, herein, we have studied *th*-BCN, as obtained by applying the SW transformation to *p*-BCN in the manner shown in Fig. 1, and systematically investigated its energetic, dynamical, mechanical, thermal, and environmental stability. Next, we have revealed its superior electronic and optical properties including sizable direct band gap, tunable anisotropic transport properties, and strong excitonic effects compared to its counterparts as the alloying offers more degrees of freedom. Finally, we have examined its potential to be a promising semiconductor for photocatalytic water splitting and switchable anisotropic 2D material for nanoelectronic and optoelectronic applications.

2. Computational methods

All the first-principles calculations were carried out using the density functional theory (DFT) with a plane-wave basis PAW pseudo-potentials [33] implemented in VASP package [34,35]. For the description of correlation and exchange interaction between electrons, we used GGA-PBE functional [36]. The kinetic energy cut-off was set at 520 eV and the Brillouin-zone (BZ) was sampled with a 16 × 16 × 1 Γ-centered *k*-point grid. To ensure the structure fully optimized, the convergence for the self-consistent energy and the maximum force were set at 10^{-5} eV and 0.01 eV/Å, respectively. For the electronic calculations, the Heyd-Scuseria-Ernzerhof screened hybrid functional (HSE06) was employed [37] as the GGA-PBE functional underestimates the band-gap energy. For the lattice dynamics calculations, we extracted the harmonic inter-atomic force constants and the phonon dispersion curves using the finite displacement method with supercell approach implemented in PHONOPY code [38] where a 4 × 3 × 1 supercell with a 2 × 2 × 1 Γ-centered *k*-point grid was used. To investigate the thermal stability, we performed *ab-initio* molecular dynamics (AIMD) calculations within the NVT ensemble (where the volume and temperature were fixed during the simulation) with the Nose thermostat [39]. The AIMD simulations were run for 10 ps with a time step of 1 fs and the temperature of the thermostat was set to 1200 K.

3. Results and discussion

3.1. Structure characterization

The optimized atomic structure of *th*-BCN is presented in Fig. 1. The unitcell consists of twelve atoms with the same number of B, C, and N atoms. The structure comprised entirely of tetragons and hexagons has three atomic layers thick where C atoms are 4-fold coordinated and sandwiched between B–N pairs. The structure belongs to a space group of *Abm*2 (No: 39). Two distinct edge directions, namely zigzag and armchair, are placed along the **a** and **b** lattice directions, respectively. The B–N pairs are 3-fold coordinated and only lie in a straight line along the armchair direction, resulting in structural anisotropy and thereby anisotropic intrinsic properties. The fully relaxed lattice parameters of $a = 4.535$ and $b = 6.284$ Å and buckling thickness of $h = 1.272$ Å are close to those of its tetrahexagonal counterparts (*th*-C [21] and *th*-BN [24]). The B–N bond length of 1.393 Å is close to that in *th*-BN (1.355 Å) [24], *h*-BN (1.451 Å) [24], and *p*-BCN (1.406 Å) [30]. The calculated B–C and C–N bond lengths (1.607 Å and 1.495 Å) are comparable with those in *p*-BCN (1.631 and 1.498 Å) [30], respectively.

3.2. Structure stability

To show the possible realization of the *th*-BCN monolayer in experiment, we further examine its energetic, dynamical, mechanical, thermal, and environment stability by evaluating formation (and cohesive) energy, lattice dynamics, elastic constants, and AIMD simulations (with and without water) respectively.

For the thermodynamic stability of *th*-BCN, we first calculated the formation energy (E_f) using the following equation;

$$E_f = (E_{BCN} - n_C\mu_C - 2n_{BN}\mu_{BN})/n \quad (1)$$

where E_{BCN} is the total unitcell energy of *th*-BCN; n_C, n_{BN}, and n denote the number of C atoms, BN pairs, and total atoms in the unitcell of *th*-BCN, respectively; μ_C and μ_{BN} correspond to the chemical potential of C atom and B–N pair, which are obtained from graphene and *h*-BN, respectively. The formation energy of *th*-BCN is found to be 1224 meV per atom, which is relatively higher than that of *p*-BCN (1204 meV per atom) and *p*-C (902 meV per atom) with respect to the corresponding hexagonal counterparts (*h*-C and *h*-BN). Moreover, the formation energy of *th*-BCN with respect to its tetrahexagonal counterparts (*th*-C and *th*-BN) is calculated as 490 meV per atom. Next, we calculated the cohesive energy (E_{coh}) using the following equation:

$$E_{coh} = \left(\sum_i n_i E_i - E_{BCN}\right)\Big/ n \quad (i = \mathrm{B},\ \mathrm{C},\ \mathrm{N}) \quad (2)$$

where E_i is the isolated atomic energy of B, C, and N; n_i denotes the number of B, C, and N atoms in the unitcell of *th*-BCN. The cohesive energy of *th*-BCN is calculated as 6.16 eV per atom, which is 0.02 eV per atom lower than that of *p*-BCN (6.18 eV per atom) [30] and comparable with the experimentally synthesized phosphorene (3.48 eV per atom) [40]. The high cohesive energy and relatively low formation energy of *th*-BCN may infer its energetic stability.

To assess the dynamical stability of the *th*-BCN monolayer, we calculated the phonon band dispersion. As presented in Fig. 2 (a), the calculated phonon spectrum appears no imaginary modes, confirming the dynamically stability. To understand the contribution of atoms to the phonon spectrum of *th*-BCN, we plotted the atom-projected phonon density-of-states (PhDOS) (Fig. 2 (a), right panel). We found that the highest phonon frequencies come from the vibration of B and N rather than C atoms, resulting in a phonon gap between 1165 and 1330 cm^{-1} frequencies. Besides, the highest phonon frequency of *th*-BCN reaches up to 1478 cm^{-1}, which is higher than that of *p*-BCN (about 1363 cm^{-1}) [30], and lower than that of *th*-C (about 1695 cm^{-1}) [21] and *th*-BN (1629 cm^{-1}) [24], and thus indicative of the robust bond network in the monolayer. Next, we calculated the dynamic stability of the *th*-BCN monolayer under extreme strain. The phonon band dispersion of *th*-BCN at 14% equi-biaxial strain were plotted in Fig. 2(b). The results show that the strained *th*-BCN monolayer also maintains the lattice dynamic stability due to the absence of imaginary mode in the phonon spectrum. We also note that the phonon instability occurs via soft modes with imaginary frequencies at 14.1% equi-biaxial strain.

The mechanical stability of *th*-BCN was further investigated by evaluating Born-Huang elastic stability criteria [41] as $C_{11}C_{22}$-C_{12}^2 >

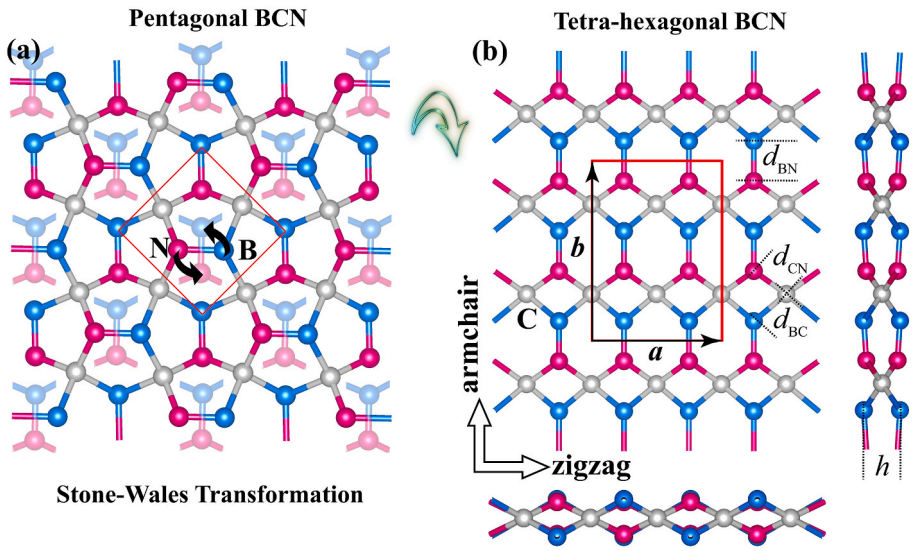

Fig. 1. Optimized atomic configurations of (a) *p*-BCN and (b) *th*-BCN monolayers. Red rectangles represent the unitcell. Blue, gray, and pink balls represent boron, carbon, and nitrogen atoms, respectively. (For interpretation of the references to colour in this figure legend, the reader is referred to the Web version of this article.)

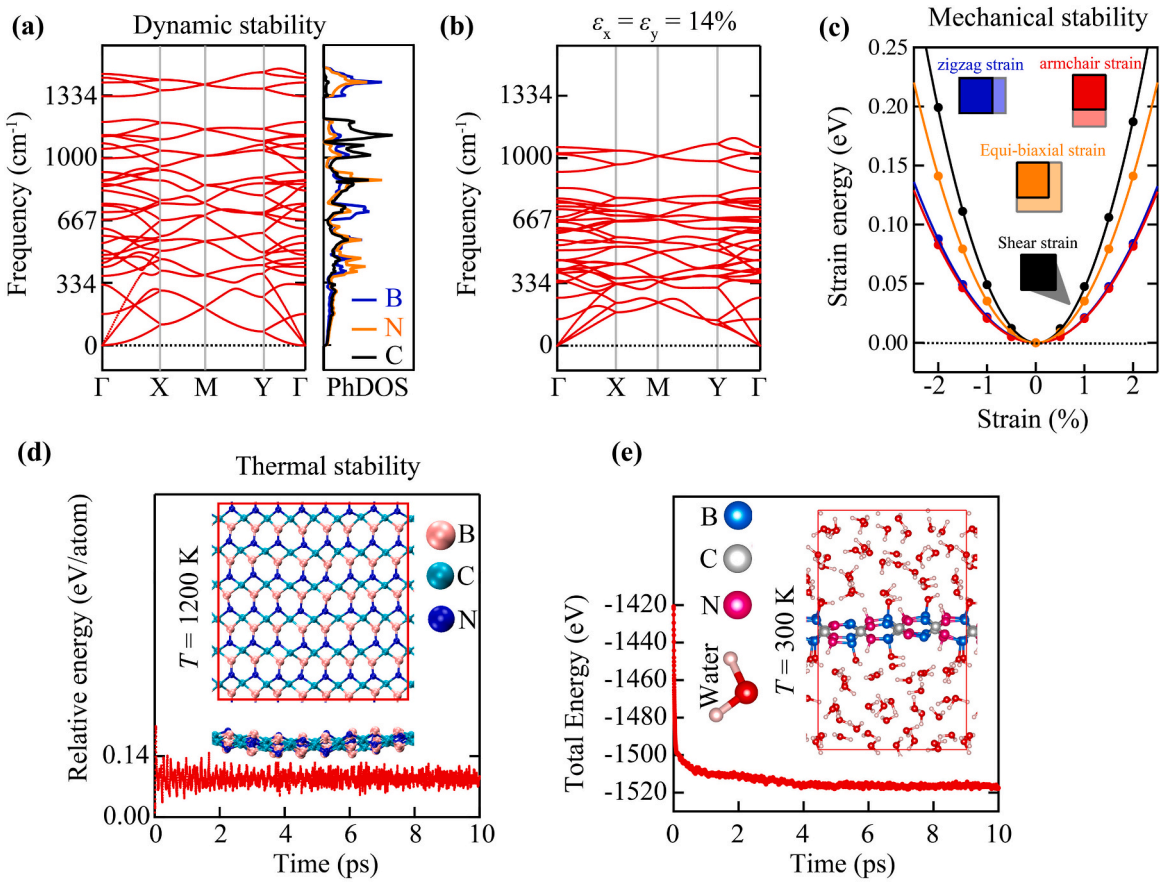

Fig. 2. (a) Calculated phonon dispersion curves with atom-projected phonon density-of-states (PhDOS) of *th*-BCN. (b) Phonon dispersion curves at 14% equi-biaxial strain. (c) Variation of strain energy with respect to applied uniaxial strain along the zigzag and armchair directions, equi-biaxial strain, and shear strain, where schematic of applied strains are depicted in inset. (d) Variation of potential energy with time at 1200 K for 10 ps where top and side views of the atomic configurations at the end of simulation time are illustrated inset. (e) Variation of total energy with time at 300 K for 10 ps where side view of the atomic configurations at the end of simulation time are illustrated inset.

0 and $C_{66} > 0$ where C_{ij} are in-plane elastic stiffness constants obtained from the second partial derivative of strain energy (E_s) as a function of strain (ϵ_{ij}) using the following equation;

$$E_s(\epsilon) = \frac{1}{2}C_{11}\epsilon_{xx}^2 + \frac{1}{2}C_{22}\epsilon_{yy}^2 + C_{12}\epsilon_{xx}\epsilon_{yy} + 2C_{66}\epsilon_{xy}^2 \quad (3)$$

We applied uniaxial strains along the zigzag and armchair directions,

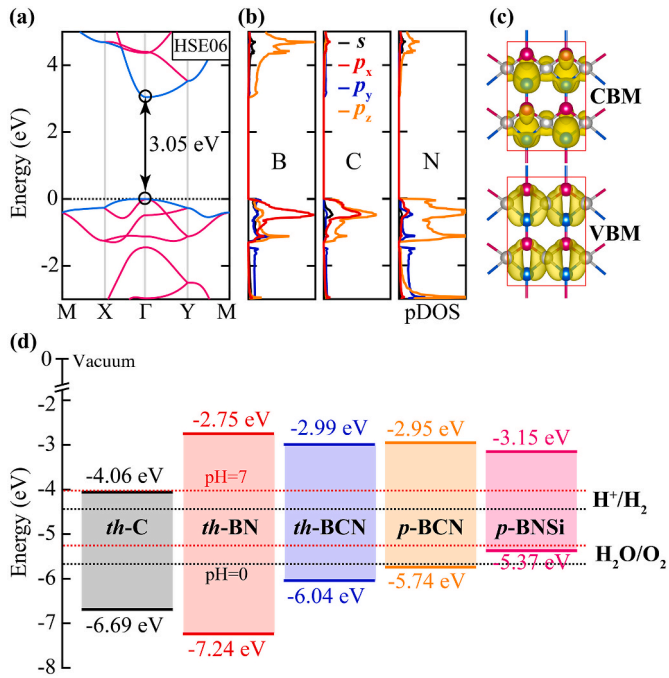

Fig. 3. (a) Calculated electronic band structure with (b) atom/orbital projected density-of-states (pDOS) at the HSE06 methodand (c) band-decomposed charge density distributions of VBM and CBM. (d) Band-edge energy positions with respect to water redox potentials for pH = 0 (dashed black line) and pH = 7 (dashed red line) for *th*-BCN, *th*-C, *th*-BN, *p*-BCN, *p*-BNSi. (For interpretation of the references to colour in this figure legend, the reader is referred to the Web version of this article.)

equi-biaxial and shear strains ranging from −2 to 2% with increment of 0.5% and plotted the E_s vs ϵ_{ij} in Fig. 2(c). From Eq. (3), we calculated the corresponding elastic constants as $C_{11} = 241.23$ N/m, $C_{22} = 230.78$ N/m, $C_{12} = 34.95$ N/m, and $C_{66} = 98.96$ N/m. These obtained elastic constants meet the elastic stability criteria for the *th*-BCN monolayer.

To further examine the thermal stability of the *th*-BCN monolayer, we performed the AIMD simulations at very high temperature (1200 K) for 10 ps on a 4 × 4 × 1 supercell containing 48 B, 48C and 48 N atoms. The evolution of energy during the AIMD simulation is presented in Fig. 2(d). It is clear that the energy of the system is almost constant with small fluctuations (83 meV per atom) resulting from the thermal vibration of atoms. As the energy is sensitive to the bond breaking or bond reformation in the structure, we ensure that the *th*-BCN retained the structural integrity at 1200 K, which is also confirmed by the structure snapshot taken at the end of the simulation. Thus, the monolayer is thermally stable up to 1200 K.

At last, we carried out the environmental stability of the *th*-BCN monolayer in liquid water. The AIMD simulations were run at 300 K for 10 ps on a 2 × 2 × 1 supercell of *th*-BCN at which the vacuum space (20 Å) was filled with water molecules of density 0.9 g/cm^3. We monitored the total energy of the system as a function of time and realized that the total energy oscillates slightly in the vicinity of −1520 eV for a long time without decay. Thus, *th*-BCN would be stable in liquid water at room temperature. More interestingly, from the snapshot of the atomic arrangement of *th*-BCN/water at the end of the simulation time (Fig. 2(e)), the interaction between *th*-BCN and water leads to the dissociation of water molecules into OH and H radicals on the B and N atoms, respectively. Thus, the dissociation of water molecules into OH and H radicals on the *th*-BCN monolayer is thermodynamically favorable, and facilitates the redox reactions of *th*-BCN with water for photocatalytic water splitting.

As a consequence, we reveal the robust stability of the *th*-BCN monolayer by evaluating the energetic, dynamical, mechanical, thermal, and environment stability. Thus, the *th*-BCN monolayer is likely to realized in experiment.

3.3. Electronic properties

We now examine the electronic properties of the *th*-BCN monolayer. The calculated electronic band structure is presented in Fig. 3(a). It can be seen that the monolayer is a direct band gap semiconductor with a band gap of 3.05 eV at the HSE06 functional method (1.88 eV at the PBE functional). The HSE06 band gap energy of *th*-BCN is in between that of *th*-C (2.63 eV) [21] and *th*-BN (4.49 eV) [24], and higher than that of *p*-BCN (2.79 eV) [30]. The valence band maximum (VBM) and the conduction band minimum (CBM) are located at the Γ point in the BZ. The results of the atom/orbital projected density-of-states (pDOS) calculations revealed that the p_z orbitals of B atoms provide the main contributions to the CBM while the VBM is composed of B-p_x, C-p_x/p_z, and dominantly N-p_z states (Fig. 3(b)). Furthermore, we plotted the band-decomposed charge density distributions for the VBM and CBM states in Fig. 3(c). Apparently, the CBM charges are mostly distributed on the B atoms while the VBM charges are mainly localized on B, C, and N atoms.

The band edge positions, in addition to band gap energy, are very important to determine potential applications of semiconductors, especially in optoelectronics. We align the band edge levels of the *th*-BCN monolayer relative to the redox levels of water and compare them with those of *th*-C, *th*-BN [24], *p*-BCN [30], and *p*-BNSi [42] in Fig. 3(d). It can be seen that the band edge positions of the *th*-BCN monolayer perfectly straddle the redox levels of water for water splitting (Fig. 3(d)). It is very encouraging to see that ternary alloying of *th*-C and *th*-BN shifts the band edge positions to more suitable places for water splitting. The energy level of VBM (about −6.04 eV) is 0.37 eV lower than the oxidation potential of H_2O/O_2 ($V_{O_2/H_2O} = -5.67$ eV) while the energy level of CBM (about −2.99 eV) is 1.45 eV higher than the reduction potential of H^+/H_2 ($V_{H^+/H_2} = -4.44$ eV). From the thermodynamic aspect, we thus revealed that the oxidation and reduction processes in *th*-BCN are energetically favored with high driving forces. The electronic band gap of *th*-BCN (3.05 eV) is also sufficiently large to overcome the water splitting reaction (> 1.23 eV). Thus, the suitable band gap and band edge positions of the *th*-BCN monolayer suggest its great potential in the application of photocatalytic water splitting.

3.4. Strain engineering of the electronic properties

As strain is an effective strategy for engineering the intrinsic properties of semiconductor materials [15], we investigated the influence of strain on the electronic band gap and band edge positions of *th*-BCN. The response of electronic band structure with band gap and band edge positions (at the HSE06 functional) to applied uniaxial strain along the zigzag and armchair directions is plotted in Fig. 4. The results show that the band gap energy decreases with increasing lattice compression and tension. Moreover, we observed that the CBM is very sensitive to zigzag tensile strain while the VBM is sensitive to armchair tensile strain, indicating that the band gap energy and band edge positions of *th*-BCN can be effectively tuned by strain applications. Although the band gap energy and band edge positions of *th*-BCN are sensitive to the uniaxial strains, the overall electronic band structure is only marginally changed. Remarkably, *th*-BCN preserves semiconducting behavior with the direct band gap under the uniaxial strain ranging from −4% to 16%.

3.5. Small effective mass and anisotropic high carrier mobility

The effective mass and carrier mobility are two main parameters to determine the electrical transport properties of the *th*-BCN monolayer. We quantitatively calculated the effective mass of electron and hole, directly related to the band wave curvature of the CBM and VBM,

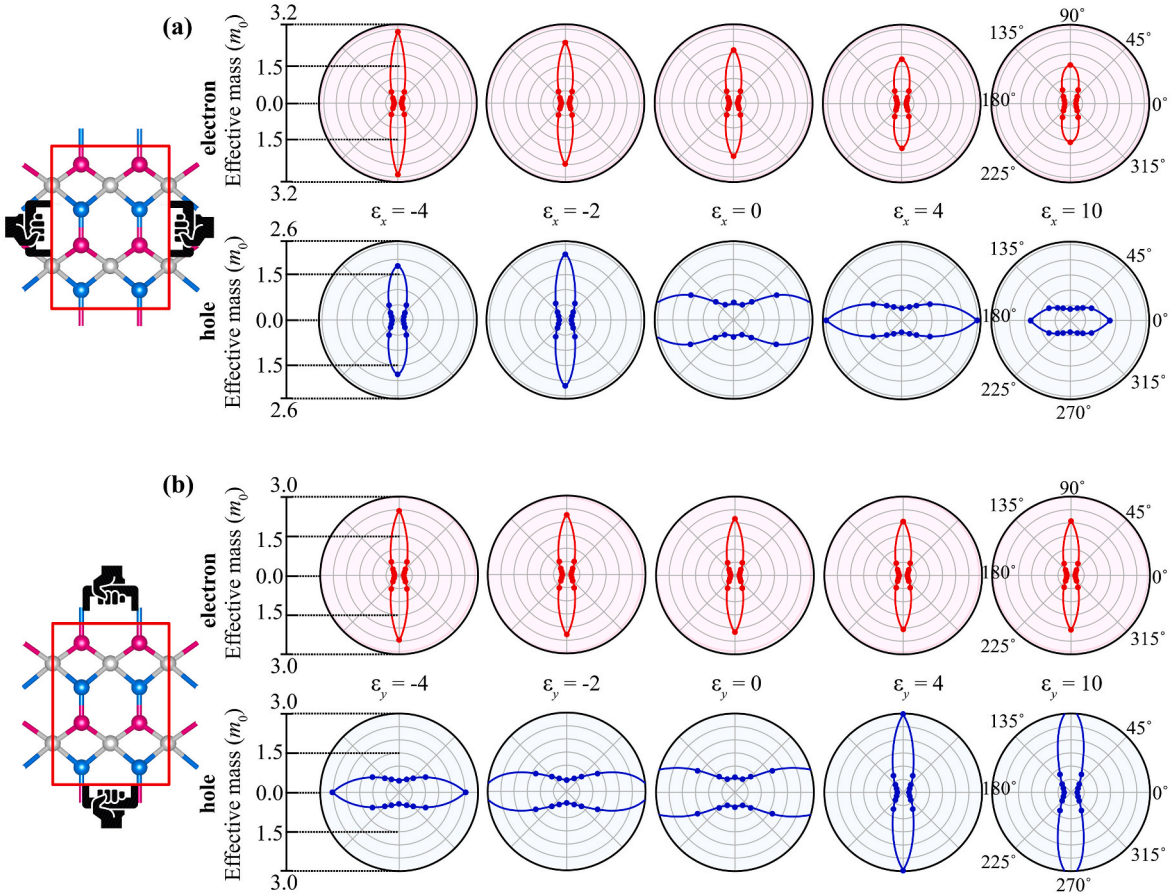

Fig. 4. Variation of electronic band structure with band gap and band edge positions with respect to water redox potentials for pH = 0 (dashed black line) and pH = 7 (dashed red line) as a function of uniaxial strain applied along the zigzag (a)-(b) and armchair direction (c)-(d). (For interpretation of the references to colour in this figure legend, the reader is referred to the Web version of this article.)

respectively, in the HSE06 electronic band structure using the following equation:

$$m^* = \hbar^2 \left(\frac{\partial^2 E(k)}{\partial k^2} \right)^{-1} \tag{4}$$

where $\hbar$, k, and $E(k)$ are the reduced Planck constant, wave vector, and corresponding electronic band energy, respectively. One can easy see from Fig. 3(a) that, at the CBM, the band dispersion along the Γ-X direction is steeper than that along the Γ-Y direction. At the VBM, the relative flatness of the band around the Γ point gives rise a large effective mass for holes. For electron, the effective mass of 0.17 m_0 (m_0 is the free electron mass) along the zigzag direction is found to be approximately 12 times smaller than that along the armchair direction. For hole, the effective mass of 0.57 m_0 along the armchair direction is almost 14 times smaller than that along the zigzag direction. Thus, the effective mass of electrons and holes are strongly anisotropic in *th*-BCN. To visualize the anisotropy in the effective mass, we plotted the effective mass of electron and hole as a function of in-plane angle (θ) in Fig. 5. Apparently, the hole effective mass displays "8" shape along the zigzag direction whereas the electron effective mass exhibits the "8" shape along the armchair direction, indicating the different direction of electron and hole concentrations. The well spatially separated charge carriers in *th*-BCN favor to effective separation of electron-hole pairs, and yields small probability of their recombination. Therefore, small and anisotropic effective mass with fast separation and low recombination of photo-induced electrons and holes in *th*-BCN are very promising for the efficiency of water splitting.

Importantly, the strain not only modulates the band gap and band edge positions of the *th*-BCN monolayer but also affects the curvature of band dispersion. To clearly show the response of the band dispersion to strain, we plotted the effective mass of electron and hole, corresponding to the curvature of the CBM and VBM, respectively, under uniaxial strain as depicted in Fig. 5. Remarkably, the effective mass of hole is rotated by exactly 90° with uniaxial compressive strain along the zigzag direction or tensile strain along the armchair direction, while the electron effective mass keeps the approximate "8" shape under these strains. We thus explored the mechanism to rotate the preferred conduction direction in *th*-BCN with a very small uniaxial strain (~2%).

Next, we calculated the carrier mobility (μ) of the *th*-BCN monolayer on the basis of deformation potential (DP) theory [43] at room temperature (300 K) using the following formula [44]:

$$\mu_i = \frac{e\hbar^3 \left(\frac{5C_i + 3C_j}{8} \right)}{k_B T (m_i^*)^{3/2} (m_j^*)^{1/2} \left(\frac{9E_{d,i}^2 + 7E_{d,i}E_{d,j} + 4E_{d,j}^2}{20} \right)} \tag{5}$$

where e and k_B are the electron charge and the Boltzmann constant, respectively. E_d is the deformation potential constant calculated by using the formula of $E_d = \partial E_{edge}/\partial \epsilon$ where E_{edge} is the energy of the VBM and CBM for holes and electrons, respectively. We calculated the band edge energies as a function of the small uniaxial strains ranging from −1 to 1% with increment of 0.5% along the deformation directions and plotted in Fig. S1 of Supporting Information. We note that the DP constant determines a feature of the coupling between electrons (or holes) and acoustic vibrations in semiconductor. For *th*-BCN, the DP constant of electron along the zigzag and armchair directions is calculated as 3.72 and 1.73 eV while that of hole is about 1.89 and 2.80 eV, respectively.

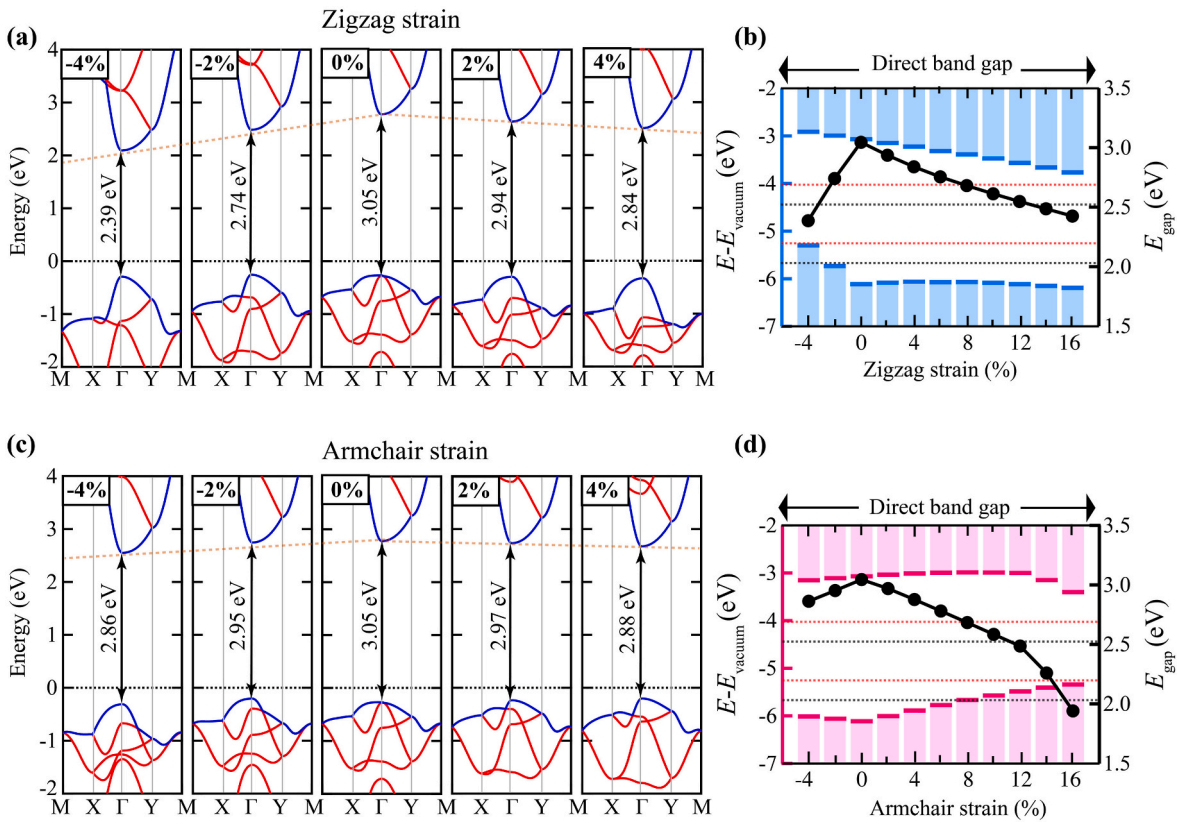

Fig. 5. Variation of electron and hole effective masses with all the spatial directions with respect to uniaxial strain along the zigzag (a) and armchair (b) directions.

Thus, the electrons are more strongly scattered by the acoustic phonon than holes in the *th*-BCN monolayer. Moreover, the electron-acoustic phonon interaction along the zigzag direction is stronger than that along the armchair direction. Thus, the DP constants of the *th*-BCN monolayer is highly direction dependent. The calculated effective mass, DP constant, and carrier mobilities are summarized in Table 1. The electron mobility along the zigzag direction is found to be 4.98×10^3 $cm^2\ V^{-1}\ s^{-1}$, which is ~9 times higher than that along the armchair direction. For holes, the mobility of 0.66×10^3 $cm^2\ V^{-1}\ s^{-1}$ along the armchair direction is ~11 times higher than that along the zigzag direction. The calculated carrier mobilities in *th*-BCN are relatively lower than those in *p*-BCN (~10^4 $cm^2\ V^{-1}\ s^{-1}$) [30].

3.6. Optical properties

We now examine the optical properties of the *th*-BCN monolayer. We calculated the frequency-dependent complex dielectric function (given as $\epsilon(\omega) = \epsilon_1(\omega) + i\epsilon_2(\omega)$ where $\epsilon_1(\omega)$ and $\epsilon_2(\omega)$ are the real and imaginary parts, respectively). Using the value of $\epsilon_1(\omega)$ and $\epsilon_2(\omega)$, we computed the optical absorption coefficient $\alpha(\omega)$ in the following equation;

$$\alpha(\omega) = \sqrt{2}\omega\left[\sqrt{\epsilon_1^2(\omega) + \epsilon_2^2(\omega)} - \epsilon_1(\omega)\right]^{1/2} \tag{6}$$

To accurately predict the optical absorption spectrum, we performed an accurate many-body approach by the quasi-particle (QP) G*W* method with the random phase approximation (RPA) [45] and the Bethe-Salpeter equation (BSE) methods [46]. We note that the G*W* + RPA takes into account electron-electron (e-e) corrections and neglects electron-hole (e-h) interactions while the G*W* + BSE properly includes both e-e and e-h interactions. Using single-shot G*W* (GW_0) approach, we calculated a direct band gap of 3.76 eV for the *th*-BCN monolayer, which is larger than that obtained from the PBE (1.88 eV) and HSE06 (3.05 eV) methods. Next, we plotted $\epsilon_2(\omega)$ and $\alpha(\omega)$ as a function of photon energy for two directions (zigzag and armchair) of polarization using the GW_0+RPA and GW_0+BSE in Fig. 6. There is a significant difference between the optical spectrum of the GW_0+RPA and GW_0+BSE. Obviously, an enormous red-shift in all the GW_0+BSE data as compared to the GW_0+RPA indicates a strong of e-h attraction in the optical spectrum of *th*-BCN. The prominent optical absorption peaks in the GW_0+BSE spectrum, which are utterly missing in the GW_0+RPA, are observed in the visible-ultraviolet region. Thus, the *th*-BCN monolayer has a strong excitonic effects. The first optical absorption peak in the GW_0+BSE spectrum is located at the photon energy of 2.78 eV in the zigzag polarization direction. This distinct excitonic peak in the visible range is below the calculated GW_0 band gap, and corresponds to the optical gap of the *th*-BCN monolayer. The second intense excitonic peak of the GW_0+BSE spectrum is observed at 3.74 eV along the armchair polarization direction. Thus, the *th*-BCN exhibits highly anisotropic optical response. Remarkably, the prominent optical absorption peaks of the GW_0+BSE spectrum in the visible-ultraviolet range can reach to ~10^6 cm^{-1}, which can be comparable to organic perovskite solar cells [47]. We further calculated the excitonic binding (E_b) energy of the lowest energy exciton peak, defined as the difference between the fundamental band gap (obtained from the GW_0) and the optical gap (obtained from the GW_0+BSE). The binding energy of the first exciton is estimated to be 0.98 eV, which is larger than that of many MX-enes [48] and lower than that in *p*-BCN (1.45 eV) [30]. As a consequence, the *th*-BCN monolayer with anisotropic optical response, high optical absorption capability in the visible range, and remarkable excitonic effects has a great potential for optoelectronic device applications.

4. Conclusion

Using first principles calculations, we have revealed the energetic, dynamical, thermal, and mechanical stability of the *th*-BCN monolayer,

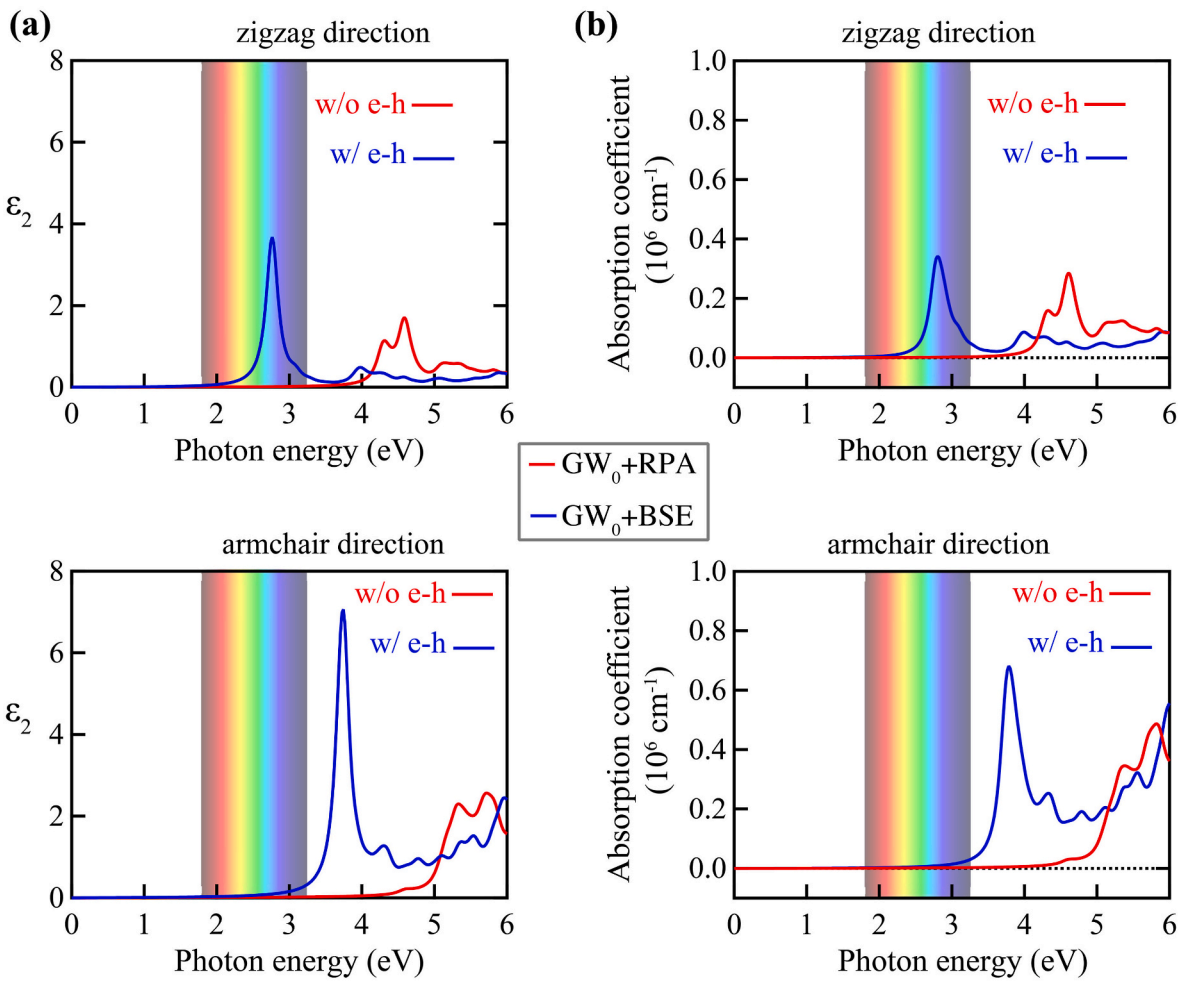

Fig. 6. (a) Imaginary part of the dielectric function and (b) optical absorption coefficient of the *th*-BCN monolayer as a function of incident light energy along the zigzag (upper panel) and armchair (lower panel) polarization directions with GW_0+RPA and GW_0+BSE methods.

Table 1
Calculated effective mass (m_x^* and m_y^*) in unit of free electron mass, in-plane elastic constants (C_x and C_y) in unit of N/m, deformation potential constants ($E_{d,\,x}$ and $E_{d,\,y}$) in unit of eV, and mobility (μ_x and μ_y) in unit of $cm^2\ V^{-1}\ s^{-1}$ at $T = 300$ K along the zigzag and armchair directions.

	m_x^*	m_y^*	C_x	C_y	$E_{d,\,x}$	$E_{d,\,y}$	μ_x	μ_y
electron	0.17	2.15	241.23	230.78	3.92	1.73	4.98×10^3	0.57×10^3
hole	8.00	0.57	241.23	230.78	1.89	2.80	0.06×10^3	0.66×10^3

suggesting that it is likely to realized in experiment. The direct and sizable band gap, appropriate band edge positions, anisotropic effective masses, and strong optical absorption capability in the visible spectrum make *th*-BCN a promising candidate for photocatalytic water splitting. We have revealed the mechanism to engineer the anisotropic transport direction of *th*-BCN by strain, promising for nanoelectronics. Having strong excitonic effects with huge excitonic binding energy and anisotropic optical response make *th*-BCN a promising candidate for optoelectronics. Therefore, we have demonstrated its potential to be a promising semiconductor for photocatalytic water splitting and switchable anisotropic 2D material for nanoelectronic and optoelectronic applications.

Credit author statement

Mehmet Emin Kilic: Conceptualization, Investigation, Draft preparation, Reviewing, Editing, and Visualization. Kwang Ryeol Lee: Reviewing and Supervision.

Declaration of competing interest

The authors declare that they have no known competing financial interests or personal relationships that could have appeared to influence the work reported in this paper.

Data availability

Data will be made available on request.

Acknowledgment

We gratefully acknowledge support by Brain Pool Program through the National Research Foundation of Korea (NRF) funded by the Ministry of Science and ICT (2020H1D3A1A02081517).

Appendix A. Supplementary data

Supplementary data to this article can be found online at https://doi.org/10.1016/j.mtphys.2022.100792.

References

[1] K.S. Novoselov, A.K. Geim, S.V. Morozov, D.-e. Jiang, Y. Zhang, S.V. Dubonos, I. V. Grigorieva, A.A. Firsov, Electric field effect in atomically thin carbon films, Science 306 (5696) (2004) 666–669.
[2] A. Nag, K. Raidongia, K.P. Hembram, R. Datta, U.V. Waghmare, C. Rao, Graphene analogues of BN: novel synthesis and properties, ACS Nano 4 (3) (2010) 1539–1544.
[3] S. Manzeli, D. Ovchinnikov, D. Pasquier, O.V. Yazyev, A. Kis, 2D transition metal dichalcogenides, Nat. Rev. Mater. 2 (8) (2017) 1–15.
[4] L. Li, Y. Yu, G.J. Ye, Q. Ge, X. Ou, H. Wu, D. Feng, X.H. Chen, Y. Zhang, Black phosphorus field-effect transistors, Nat. Nanotechnol. 9 (5) (2014) 372–377.
[5] A.J. Mannix, Z. Zhang, N.P. Guisinger, B.I. Yakobson, M.C. Hersam, Borophene as a prototype for synthetic 2D materials development, Nat. Nanotechnol. 13 (6) (2018) 444–450.
[6] P. Vogt, P. De Padova, C. Quaresima, J. Avila, E. Frantzeskakis, M.C. Asensio, A. Resta, B. Ealet, G. Le Lay, Silicene: compelling experimental evidence for graphenelike two-dimensional silicon, Phys. Rev. Lett. 108 (15) (2012): 155501.
[7] J.R. Schaibley, H. Yu, G. Clark, P. Rivera, J.S. Ross, K.L. Seyler, W. Yao, X. Xu, Valleytronics in 2D materials, Nat. Rev. Mater. 1 (11) (2016) 1–15.
[8] H. Li, Z. Song, X. Zhang, Y. Huang, S. Li, Y. Mao, H.J. Ploehn, Y. Bao, M. Yu, Ultrathin, molecular-sieving graphene oxide membranes for selective hydrogen separation, Science 342 (6154) (2013) 95–98.
[9] F. Song, X. Hu, Exfoliation of layered double hydroxides for enhanced oxygen evolution catalysis, Nat. Commun. 5 (1) (2014) 1–9.
[10] H. Zhang, Ultrathin two-dimensional nanomaterials, ACS Nano 9 (10) (2015) 9451–9469.
[11] S. Zhang, J. Zhou, Q. Wang, X. Chen, Y. Kawazoe, P. Jena, Penta-graphene: a new carbon allotrope, Proc. Natl. Acad. Sci. USA 112 (8) (2015) 2372–2377.
[12] M.E. Kilic, K.-R. Lee, Penta carbides: two-dimensional group-IV semiconductors containing C2 dimers for nanoelectronics and photocatalytic water splitting, Phys. Rev. Mater. 5 (6) (2021): 065404.
[13] Y. Shao, M. Shao, Y. Kawazoe, X. Shi, H. Pan, Exploring new two-dimensional monolayers: pentagonal transition metal borides/carbides (penta-TMB/Cs), J. Math. Chem. A 6 (22) (2018) 10226–10232.
[14] J. Li, X. Fan, Y. Wei, G. Chen, Penta-BxNy sheet: a density functional theory study of two-dimensional material, Sci. Rep. 6 (1) (2016) 1–9.
[15] M.E. Kilic, K.-R. Lee, Four-penta-graphenes: novel two-dimensional fenestrane-based auxetic nanocarbon allotropes for nanoelectronics and optoelectronics, Carbon 195 (2022) 154–164.
[16] A.D. Oyedele, S. Yang, L. Liang, A.A. Puretzky, K. Wang, J. Zhang, P. Yu, P. R. Pudasaini, A.W. Ghosh, Z. Liu, PdSe2: pentagonal two-dimensional layers with high air stability for electronics, J. Am. Chem. Soc. 139 (40) (2017) 14090–14097.
[17] P.K. Cheng, S. Liu, S. Ahmed, J. Qu, J. Qiao, Q. Wen, Y.H. Tsang, Ultrafast Yb-doped fiber laser using few layers of PdS2 saturable absorber, Nanomaterials 10 (12) (2020) 2441.
[18] M. Bykov, E. Bykova, A.V. Ponomareva, F. Tasnadi, S. Chariton, V.B. Prakapenka, K. Glazyrin, J.S. Smith, M.F. Mahmood, I.A. Abrikosov, Realization of an ideal cairo tessellation in nickel diazenide NiN2: high-pressure route to pentagonal 2D materials, ACS Nano 15 (8) (2021) 13539–13546.
[19] J.I. Cerdá, J. Sławińska, G. Le Lay, A.C. Marele, J.M. Gómez-Rodríguez, M. E. Dávila, Unveiling the pentagonal nature of perfectly aligned single-and double-strand Si nano-ribbons on Ag (110), Nat. Commun. 7 (1) (2016) 1–7.
[20] B. Ram, H. Mizuseki, Tetrahexcarbon: a two-dimensional allotrope of carbon, Carbon 137 (2018) 266–273.
[21] M.E. Kilic, K.-R. Lee, Tuning the electronic, mechanical, thermal, and optical properties of tetrahexcarbon via hydrogenation, Carbon 161 (2020) 71–82.
[22] M.E. Kilic, K.-R. Lee, Tetrahex carbides: two-dimensional group-IV materials for nanoelectronics and photocatalytic water splitting, Carbon 174 (2021) 368–381.
[23] M.E. Kilic, K.-R. Lee, Novel Two-dimensional Group-IV carbides containing C2 dimers: sizable direct band gap, high carrier mobility, and anisotropic properties for nanoelectronics, Carbon 181 (2021) 421–432.
[24] M.E. Kilic, K.-R. Lee, Novel two-dimensional tetrahexagonal boron nitride with a sizable band gap and a sign-tunable Poisson's ratio, Nanoscale 13 (20) (2021) 9303–9314.
[25] M.E. Kilic, S.E. Rad, S. Jahangirov, Two-dimensional tetrahexagonal CX2 (X = P, as, Sb) semiconductors for photocatalytic wWter splitting under visible light, Phys. Rev. Mater. 6 (3) (2022): 035402.
[26] M.E. Kilic, S.E. Rad, S. Ipek, S. Jahangirov, Boron-pnictogens: highly anisotropic two-dimensional semiconductors for nanoelectronics and optoelectronics, Phys. Rev. Mater. 6 (6) (2022): 064007.
[27] C.N.R. Rao, M. Chhetri, Borocarbonitrides as metal-free catalysts for the hydrogen evolution reaction, Adv. Mater. 31 (13) (2019): 1803668.
[28] M. Chhetri, S. Maitra, H. Chakraborty, U.V. Waghmare, C. Rao, Superior performance of borocarbonitrides, $B_xC_yN_z$, as stable, low-cost metal-free electrocatalysts for the hydrogen evolution reaction, Energy Environ. Sci. 9 (1) (2016) 95–101.
[29] K. Zhao, Y. Guo, Y. Shen, Q. Wang, Y. Kawazoe, P. Jena, Penta-BCN: a new ternary pentagonal monolayer with intrinsic piezoelectricity, J. Phys. Chem. Lett. 11 (9) (2020) 3501–3506.
[30] M.E. Kilic, K.-R. Lee, Two-dimensional ternary pentagonal BCN: a promising photocatalyst semiconductor for water splitting with strong excitonic effects, Phys. Rev. Appl. 18 (1) (2022): 014066.
[31] S.B. Sharma, K. Santosh, D. Paudyal, Enhanced optoelectronic and elastic responses in fluorinated penta-BCN, Appl. Surf. Sci. 593 (2022): 153239.
[32] A. Lopez-Bezanilla, P.B. Littlewood, Semimetallicity and electron-hole liquid in two-dimensional C and BN based compounds, Phys. Rev. Mater. 5 (1) (2021): 014006.
[33] P.E. Blöchl, Projector augmented-wave method, Phys. Rev. B 50 (24) (1994): 17953.
[34] G. Kresse, J. Hafner, Norm-conserving and ultrasoft pseudopotentials for first-row and transition elements, J. Phys. Condens. Matter 6 (40) (1994) 8245.
[35] G. Kresse, D. Joubert, From ultrasoft pseudopotentials to the projector augmented-wave method, Phys. Rev. B 59 (3) (1999) 1758.
[36] J.P. Perdew, K. Burke, M. Ernzerhof, Generalized gradient approximation made simple, Phys. Rev. Lett. 77 (18) (1996) 3865.
[37] J. Heyd, G.E. Scuseria, M. Ernzerhof, Hybrid functionals based on a screened coulomb potential, J. Chem. Phys. 118 (18) (2003) 8207–8215.
[38] L. Chaput, A. Togo, I. Tanaka, G. Hug, Phonon-phonon interactions in transition metals, Phys. Rev. B 84 (9) (2011): 094302.
[39] S. Nosé, A unified formulation of the constant temperature molecular dynamics methods, J. Chem. Phys. 81 (1) (1984) 511–519.
[40] V. Vierimaa, A.V. Krasheninnikov, H.-P. Komsa, Phosphorene under electron beam: from monolayer to one-dimensional chains, Nanoscale 8 (15) (2016) 7949–7957.
[41] M. Born, K. Huang, Dynamical Theory of Crystal Lattices, Oxford, 1954.
[42] M.J. Varjovi, M.E. Kilic, E. Durgun, Ternary pentagonal BNSi monolayer: two-dimensional structure with potentially high carrier mobility and strong excitonic effects for photocatalytic applications, Phys. Rev. Mater. 6 (3) (2022): 034004.
[43] J. Bardeen, W. Shockley, Deformation potentials and mobilities in non-polar crystals, Phys. Rev. 80 (1) (1950) 72.
[44] H. Lang, S. Zhang, Z. Liu, Mobility anisotropy of two-dimensional semiconductors, Phys. Rev. B 94 (23) (2016): 235306.
[45] H. Ehrenreich, M.H. Cohen, Self-consistent field approach to the many-electron problem, Phys. Rev. 115 (4) (1959) 786.
[46] M. Shishkin, G. Kresse, Implementation and performance of the frequency-dependent GW method within the PAW framework, Phys. Rev. B 74 (3) (2006): 035101.
[47] N.J. Jeon, J.H. Noh, Y.C. Kim, W.S. Yang, S. Ryu, S.I. Seok, Solvent engineering for high-performance inorganic–organic hybrid perovskite solar cells, Nat. Mater. 13 (9) (2014) 897–903.
[48] Z. Jiang, Z. Liu, Y. Li, W. Duan, Scaling universality between band gap and exciton binding energy of two-dimensional semiconductors, Phys. Rev. Lett. 118 (26) (2017): 266401.